Strain annealing of SiC nanoparticles revealed through Bragg coherent diffraction imaging for quantum technologies

S. O. Hruszkewycz,[1] S. Maddali,[1] C. P. Anderson,[2,3] W. Cha,[4] K. C. Miao,[3] M. J. Highland,[1] A. Ulvestad,[1] D. D. Awschalom,[3,5] and F. J. Heremans[3,5]

[1]*Materials Science Division, Argonne National Laboratory, Argonne, Illinois 60439, USA*
[2]*Department of Physics, University of Chicago, Chicago, Illinois 60637, USA*
[3]*Institute for Molecular Engineering, University of Chicago, Chicago, Illinois 60637, USA*
[4]*X-ray Science Division, Argonne National Laboratory, Argonne, Illinois 60439, USA*
[5]*Institute for Molecular Engineering & Materials Science Division, Argonne National Laboratory, Argonne, Illinois 60439, USA*

(Received 17 February 2018; published 2 August 2018)

The crystalline strain properties of nanoparticles have broad implications in a number of emerging fields, including quantum and biological sensing in which heterogeneous internal strain fields are detrimental to performance. Here we used synchrotron-based Bragg coherent x-ray diffraction imaging (BCDI) to measure three-dimensional lattice strain fields within individual 3C-SiC nanoparticles, a candidate host material for quantum sensing, as a function of temperature during and after annealing up to 900 °C. We observed pronounced homogenization of the initial strain field at temperatures above 500 °C, and we find that the surface layers and central volumes of the nanoparticles reduce strain at similar rates, suggesting a uniform healing mechanism. Thus, we attribute the observed strain homogenization to activation of mobile point defects that annihilate and improve the overall quality of the crystal lattice. This work also establishes the feasibility of performing BCDI at high temperatures (up to 900 °C) to map structural hystereses relevant to the processing of quantum nanomaterials.

DOI: 10.1103/PhysRevMaterials.2.086001

I. INTRODUCTION

Wide bandgap semiconductors imbued with low concentrations of specific types of defects in an otherwise high-quality crystal form the foundation of power electronics, optoelectronics, as well as optical quantum devices and sensors. Silicon carbide (SiC) is one such wide-bandgap semiconductor that is common in high power/high temperature electronics [1,2] and micro-electro-mechanical systems [3] due to its unique combination of excellent chemical, electronic, and mechanical properties. Specifically, SiC nanomaterials find many uses ranging from abrasives and ceramic plates [4], to hosting single-photon emitters as potential fluorescent biomarkers [5].

More recently, SiC has shown promise as an excellent host lattice for quantum applications with multiple optically active point defects [5–7] analogous to the nitrogen-vacancy (NV) center in diamond [8], as it offers a crystalline platform for well-isolated, optically active defects for quantum technologies, including quantum information processing, secure communication, and nanoscale sensing [9,10]. Moreover, the multiple polytypes of SiC [11] allow for a variety of bandgaps [12], electronic properties [13], and optically emitting defects [14], and make SiC an attractive and versatile material for next-generation quantum devices. In this work, we focus on SiC nanoparticles as a model system for understanding annealing dynamics, in the context of nanoscale quantum sensing where SiC potentially has distinct advantages in scalability and nanofabrication methods compared to other materials such as diamond.

The functioning mechanism of nanoparticle-based quantum sensors for magnetometry, thermometry, and so on, relies on subtle changes to the spin-dependent photoluminescence from optically active point defects within the host nanocrystal as a result of the environment outside the nanoparticle. Because large ensembles of such point defects are embedded within a single nanocrystal, it is imperative that the crystal be otherwise free of inhomogeneities. For example, remnant strain fields and uncontrolled defect populations resulting from the nanoparticle fabrication process should be removed to ensure as high-quality of a crystal as possible prior to processing the material for quantum applications.

Such strain inhomogeneities can randomly perturb the optical transition frequencies, limit coupling to optical cavities and photostability, as well as broaden spin resonance transitions [15,16]. These detrimental effects could ultimately limit the sensitivity that can be achieved for nanoscale sensing or readout fidelities for quantum information processing and communication. For example, in the case of 3C-SiC, isolated divacancy defects have been observed with spin coherence times approaching 1 ms, which makes these defects, along with a better understanding of the excited state structure, amenable to advanced quantum optic protocols [17]. However, the optical linewidths of defects in 3C-SiC material are five to ten times broader than their 4H- and 6H-SiC counterparts, due largely to impurities and high crystalline strain in the growth of 3C-SiC material. High strain also induces orbital mixing, hindering the effectiveness of cycling transitions used for high contrast readout protocols.

This work is also motivated by the need to understand strain annealing characteristics in bulk SiC for broader quantum technologies. In bulk, CVD-grown SiC, remnant strain fields surrounding single active defects can perturb the optical transition frequencies by several GHz. While these local perturbations can be accounted for using electric-fields [18], the ability to improve the crystal quality of bulk SiC is necessary for these systems to scale for a number of applications, including efficiently coupling to optical cavities. Furthermore, strain can also adversely affect the quantum efficiency of light emitting systems [16], which generally reduces photoluminescence and photostability from the defect centers, limiting the signal contrast needed for both quantum information protocols and nanoscale sensing applications. The evolution of local strain fields in SiC nanoparticles under different annealing conditions therefore may also inform processing strategies for a number of SiC applications.

Here we explore the intrinsic strain fields within commercial SiC nanoparticles (3C, cubic structure polytype) and report significant improvements in the internal strain homogeneity of individual particles achieved during annealing to temperatures greater than 500 °C where point defect mobility in SiC is expected to activate. These insights were made possible with *in situ* x-ray Bragg coherent diffraction imaging (BCDI), and suggest a route towards processing inexpensive SiC nanoparticles into viable hosts for quantum sensing. Furthermore, these techniques could impact other applications that use SiC nanoparticles and have specific morphology and strain homogeneity requirements such as biomarkers, where smoother particles are more biocompatible and internal strain impacts performance [16,19].

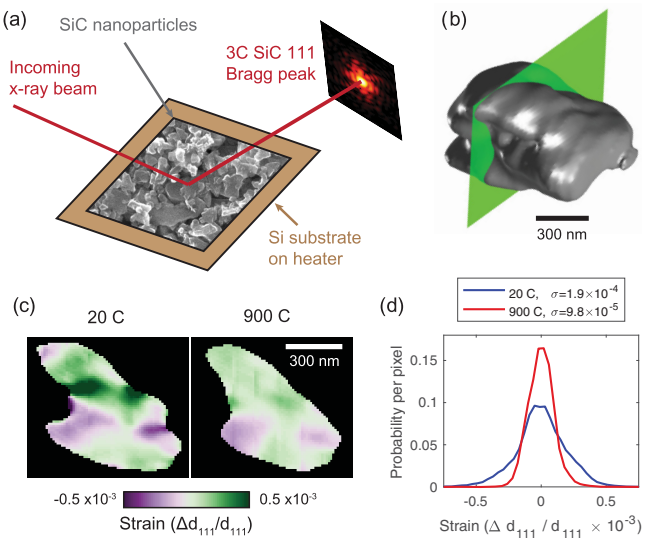

FIG. 1. A schematic of the experiment is shown (a) in which a coherent Bragg peak from a single 3C SiC nanoparticle in an ensemble deposited on a Si substrate is measured. The heater below the substrate enables temperature-dependent measurements in an atmosphere of flowing Ar gas. Using BCDI, the Bragg peak measurements are inverted to real-space 3D images that reveal the shape of the particle [gray isosurface in (b)]. Additionally, BCDI gives the internal strain within the particle. The strain fields of this particle along the green cut plane in (b) are shown in (c) at two different temperatures along with histograms (d) of the pixel-wise strain values of the images that show evidence of strain homogenization at high temperature.

II. METHODS

The 3C-SiC nanoparticle samples used in this study were purchased commercially from *Nano*Amor. The nanoparticles were suspended in isopropyl alcohol and drop-cast onto a silicon wafer with a sufficient area coverage for BCDI experiments. The samples were mounted in a custom-built heater/gas-flow cell compatible with an x-ray goniometer in a helium gas environment, as in previous experiments [20]. The BCDI experiments were performed at the Sector 34-ID-C synchrotron beamline at the Advanced Photon Source at Argonne National Laboratory using a focused 9 keV coherent x-ray beam.

A single suitable nanoparticle was measured as a function of temperature on each of five substrates prepared for this study. BCDI measurements were performed at the SiC 111 Bragg condition [see Fig. 1(a)] with an x-ray area detector. The measurements entailed scanning the angle of the sample relative to the incident x-ray beam in fine angular steps about the Bragg peak of an individual nanoparticle and recording the resulting series of coherent x-ray diffraction patterns. From such a data set, three dimensional (3D) strain-sensitive images of the individual SiC nanoparticle of interest were generated using standard BCDI image reconstruction methods described elsewhere [21,22].

As shown in Figs. 1(b) and 1(c), a single BCDI image reconstruction yields both the external shape of the nanocrystal as well as the 3D internal spatial distribution of a component of the strain tensor. In this experiment, the measurement is sensitive to the lattice expansion/contraction along of the (111) lattice planes that diffract into the detector. This component of strain is hereafter referred to as $\Delta d_{111}/d_{111}$. In the following analysis, we report the strain homogeneity of a given particle via the standard deviation (σ_{str}) of the probability histogram of $\Delta d_{111}/d_{111}$ of all pixels in the 3D image of the particle. (In a later section, we explore the spatial distribution of this quantity.) Examples of such histograms are shown in Fig. 1(d) with σ_{str} reported for one SiC nanoparticle measured at two temperatures. The σ_{str} metric conveniently captures the homogenization of the internal strain state of the particle at higher temperatures that can be visually identified in the spatial strain images [Fig. 1(c)].

Using the heater stage, repeated BCDI measurements of a given particle were performed at a series of temperatures from 20 °C up to temperatures as high as 900 °C. At a given temperature, after waiting ∼30 minutes for equilibration, BCDI scans lasting ∼60 s were repeated 10 to 15 times to produce a series of 3D images from which a mean σ_{str} and uncertainty were derived. The uncertainties are reported as one standard deviation of σ_{str} from the set of images measured at a given temperature. We observed that the no significant strain annealing takes place during the 10 to 15 minutes of measurement time, thus we take these uncertainties to represent experimental errors under each measurement condition (such as heater stage drift) of a static-structured sample. A ramp rate of 10–15 °C per minute was used to reach sequential

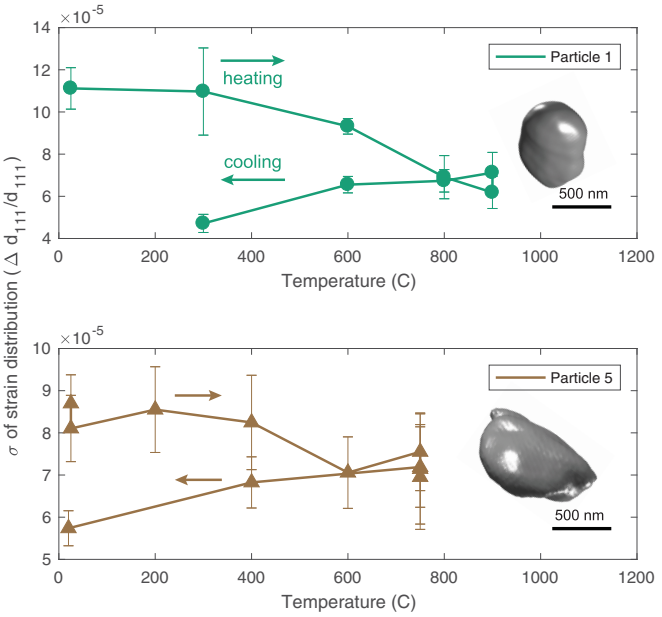

FIG. 2. The evolution of the homogeneity of the internal strain field (σ_{str}) of two of the particles in this study (top and bottom panels) is plotted as a function of temperature, showing a hysteresis due to strain annealing at high temperatures.

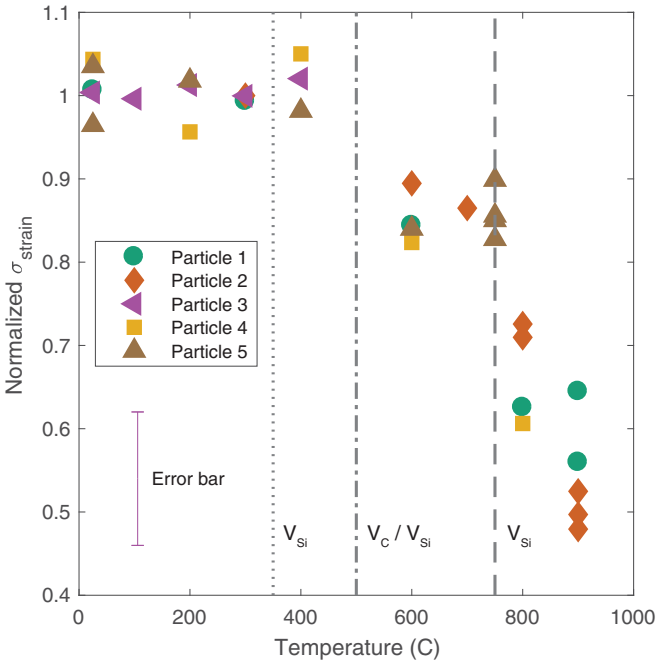

FIG. 3. Normalized σ_{str} of all five particles during heating (measurements made upon cooling excluded). Vertical lines correspond to temperatures where we observe a two-stage annealing effect likely to correspond to the activation of certain point defects mobilizing in the crystal. The average error bar (one standard deviation) is depicted in the bottom left corner.

temperatures while tracking the particle. For the five particles investigated in this study, BCDI measurements were performed up to a maximum temperature of 900, 900, 400, 800, and 750 °C, respectively, in temperature increments of 100–300 °C. With the exception of particle 4, BCDI measurements were also performed upon cooling to room temperature to record the hysteresis of the strain states of the particles. The morphology of two of these particles in their final measured states is featured in Figs. 2(a) and 2(b) (insets), with the remainder shown before and after annealing in the Appendix showing a particle diameter range of 500–1500 nm.

Also shown in the Appendix are scanning electron microscopy (SEM) images of (a) an as-prepared SiC sample for BCDI, and (b) the sample from which particle 4 was measured after it was annealed to 800 °C. These SEM images show that the post-annealed SiC nanoparticles have a morphology that is characteristically smoother than the initial state. This effect can also be observed by comparing the BCDI images (see Appendix) of the initial and final states of the SiC nanoparticles in this study that were annealed to maximum temperatures above 400 °C. Such smoothing can be beneficial to certain applications of SiC nanoparticles, for example, in biosensing or nanonoabrasives, however, for the remainder of the paper we focus on the observed changes in strain within the particles.

III. HIGH TEMPERATURE STRAIN ANNEALING

Temperature/strain hysteresis loops of two of these particles are shown in Fig. 2. In this plot, we observe that at temperatures above 500 °C, σ_{str} decreases, and that the annealed strain state persists upon cooling. This was found to be true for all particles studied for which final room temperature measurements were made. Strain hysteresis loops for all five particles as well as plots of σ_{str} as a function of time for all particles are shown in the Appendix.

A plot of the reduced data for all particles in terms of the normalized quantity $\sigma_{str}(T)/\sigma_{str}^{max}$ is presented in Fig. 3. For clarity, cooling measurements are excluded, as the final internal strain state for all particles was found not to vary significantly from the strain state observed at the highest temperature. From this plot, we find that particle strain states are unaffected at temperatures up to 400 °C (apart from one anomalous data point, discussed in the Appendix and not shown here). However, at temperatures between 600–900 °C, we find improvements in the relative homogeneity of the internal strain fields of the particles of order 15–50% upon annealing.

This two-stage strain annealing behavior can possibly be attributed to the activation of mobile point defects in 3C-SiC. Electron-paramagnetic-resonance experiments on bulk 3C-SiC have found pronounced silicon vacancy annealing at a temperature of 350 °C and 750 °C and carbon vacancy annealing at 500 °C [23–25] (indicated as vertical dashed and dotted lines in Fig. 3). Other studies also indicate that this temperature range is associated with vacancy annealing in bulk 3C-SiC [26] and with changes in the stress state of polycrystalline 3C-SiC thin films grown on silicon [27]. Additionally, the annealing of more complex point defect structures, such as the vacancy antisite complexes are also thought to occur in this temperature range [26,28]. We note that signatures of dislocations were not found in any of the BCDI images [29], such that strain annealing via dislocation motion can be ruled

out. We also find that isolated or widely spaced stacking faults are not readily identifiable, as in other BCDI work on more perfect gold nanocrystals [30], though their presence cannot be ruled out entirely given the nonuniformity of the strain field. Thus, we posit that mobile point defects account for the high temperature improvements in strain homogeneity within the particles measured here.

Mobile point defects can relieve strain by, for example, the combination of an interstitial defect with a vacancy or by vacancy migration to free surfaces. We observed that σ_{str} decreased by an average value of 5.5×10^{-5} in the SiC nanoparticles. Though this strain homogenization could take place by many mechanisms, we consider the two above-mentioned simplified cases to roughly estimate the number of point defects that might be annihilated during annealing. The fractional relaxation volume per atomic site associated with a single lattice vacancy is relatively small (of order ~ -0.3 in a metal [31,32]), and that of an interstitial point defect is considerably larger and of opposite sign ($\sim$2 for a Si interstitial in 3C-SiC [33]). Thus, in a nonionic crystal, migration of vacancies to a surface expands the lattice, while recombination of vacancy-interstitial Frenkel pairs contracts the lattice, and both mechanisms can account for changes in local strain fields [32]. We follow the treatment of the authors of Ref. [32] to equate a change in σ_{str} to a change in concentration of point defects, presuming σ_{str} can be equated to a hydrostatic strain using the relaxation volume numbers mentioned above as estimates. We find that, on average, the recombination of eight vacancy-interstitial pairs or the removal of 30 vacancies per image pixel ($\sim$1700 nm^3) due to annealing can account for the measured degree of strain reduction. Due to the fact that in our calculation of the density of mobile defects we assume that all the observed strain is hydrostatic, the resulting estimates represent a maximum upper bound on the number of mobile defects activated during the annealing. Access to multiple Bragg peaks from the same particle could corroborate this assumption, but was experimentally not feasible in this case. We also note that without more detailed knowledge of the processing history of the particles, it is difficult to estimate the initial defect concentration in the particle with this simple model.

The fabrication of low-cost SiC nanoparticles likely results in a large range of defects and inhomogeneities intrinsic to the synthesis process. As a result, vacancies and interstitials can be expected, along with other possible structural defects such as stacking faults and polytype inclusions. The fact that inhomogeneous strain fields remained in the particles annealed to 900° C suggests that further strain homogenization requires more annealing time or higher temperatures that activate more healing mechanisms. Additionally, we note that further insight into these mechanisms could be gained by performing BCDI experiments at other Bragg peaks that have different structural sensitivity, such as discriminating different SiC polytypes. Furthermore, high-temperature BCDI experiments opens the door to imaging experiments preferentially sensitive to specific types of point defects that are expected to have asymmetric associated strain fields.

Nonetheless, in this study a mean final value of $\sigma_{str} = 6.6 \times 10^{-5}$ was found for the particles annealed to temperatures up to 900 °C. We find pronounced strain homogenization of the nanocrystals at this temperature with an observed decrease in σ_{str} of up to 50%. This result not only sheds light as to the strain healing mechanism, but can also potentially account for expected improvements in line-width of spin defect resonance transitions in SiC after annealing, analogous to those seen in bulk diamond [15,16].

Isolated divacancy defects have been observed in 3C-SiC with spin coherence times approaching 1 ms, which makes these defects, along with a better understanding of the excited state structure, amenable to advanced quantum optic protocols [17]. However, the optical linewidths of defects in 3C-SiC material are five to ten times broader than their 4H- and 6H-SiC counterparts, due largely to impurities and high crystalline strain in the growth of 3C-SiC material. High strain also induces orbital mixing, hindering the effectiveness of cycling transitions used for high contrast readout protocols.

Finally, we note that other polytypes of SiC, namely 4H and 6H, are also being explored as candidate materials for nanoparticle quantum sensing and may provide certain benefits because of the availability of different point defect symmetries. Preliminary *in situ* BCDI experiments on 6H-SiC suggest that the structural healing mechanisms observed in this work on 3C-SiC also apply to other polytypes and nanoparticles synthesized via other methods.

IV. SURFACE STRAIN AND CHEMISTRY DURING ANNEALING

Here we examine the relationship of the strain state in the near-surface region of the particles as compared to their interior

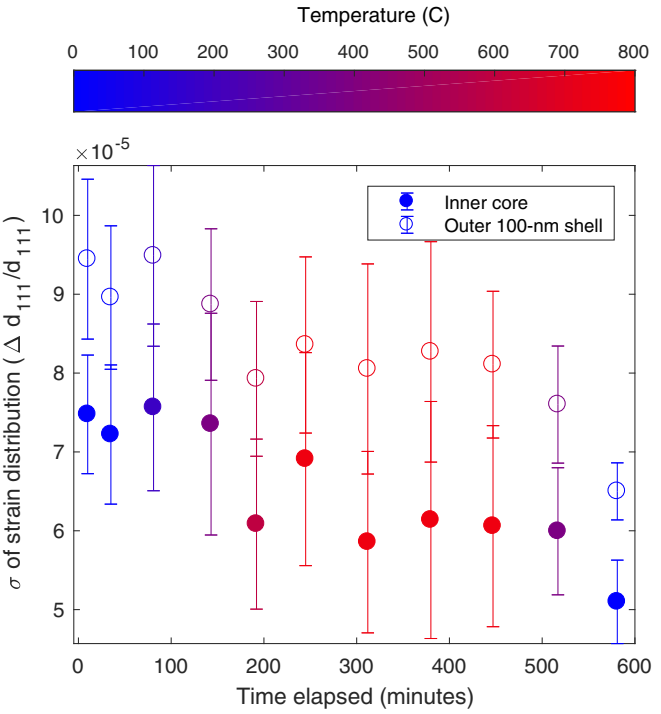

FIG. 4. A comparison of strain in the 100-nm-deep surface layer of the particles as compared to the central core of is shown for Particle 5 as an example. The same analysis was done for all particles. As is shown, the strain in the shell is higher than that of the core at all stages of annealing, and that both strains decrease together. The ratio of the core/shell strain distributions is shown in Fig. 5.

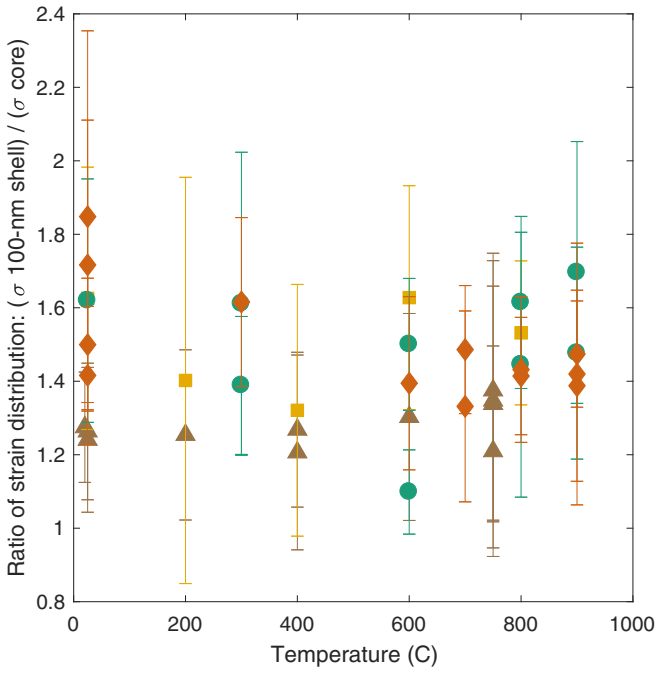

FIG. 5. The ratio of strain distribution width of the outer ∼100-nanometer-deep surface layer compared to the central core for all particles heated above 400 °C (symbol color legend as in Fig. 3).

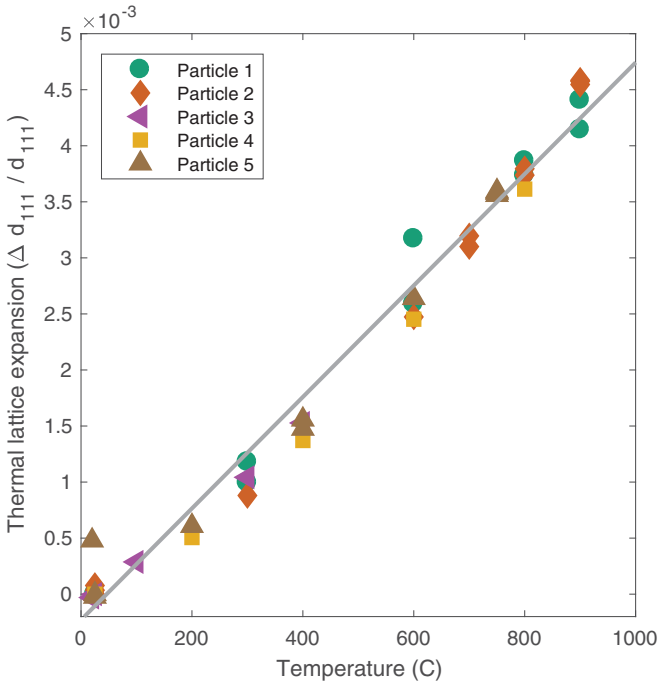

FIG. 6. Relative changes in (111) lattice spacing as a function of temperature for all particles from which a coefficient of thermal expansion was extracted by linear fitting of the data (gray line).

volumes. We separately applied the strain distribution analysis described above to the 100-nm-deep surface layer (the "shell") of the particle and the remaining inner volume (the "core") at each temperature state. The results for Particle 5 are shown in Fig. 4, which represent the trend seen for all particles.

We find that at all stages of annealing, the shell is consistently more strained than the core. However, the levels of strain of both the core and the shell decrease at similar rates at higher annealing temperatures, as shown in Fig. 4. As a result, we find that the ratio of shell/core strain remains constant throughout the process (Fig. 5) while the particles undergo an overall reduction of strain. This suggests that the mechanism of strain reduction acts homogeneously throughout the particles and is bulk-like rather than surface-driven, as would be the case for structural healing via annihilation of existing point defects.

This viewpoint is corroborated by ensemble Raman spectroscopy measurements (see Appendix) that were performed to identify possible changes in the chemical makeup of the surface of the particles before and after annealing. The pre and postannealed sample Raman spectra did not differ appreciably and showed no evidence of surface carbonization in the postannealed samples. Furthermore, residual gas analysis of the exhaust from the sample heater chamber revealed no significant change as a function of temperature during the BCDI measurements.

V. LATTICE EXPANSION AND QUANTUM SENSING

The temperature-dependent BCDI measurements discussed above can also be used to measure changes in the overall (111) lattice constant of the particles, providing a direct measurement of the room temperature lattice constant and the coefficient of thermal expansion (CTE), which plays a role in quantum sensing. The values of the (111) 3C SiC lattice constant were extracted for each particle temperature from the position of the Bragg peak in the area detector. The room temperature mean (111) lattice parameter for 3C-SiC was measured to be 2.5146 ± 0.0068 Å for the five particles, similar to the value of 2.5109 Å found in the literature [34]. The relative expansion of the lattice ($\Delta d_{111}/d_{111}^{RT}$) of all the temperatures and particles is shown in Fig. 6. A linear fit to these data gives a CTE of 4.97×10^{-6}, consistent with literature values [35].

As thermometry protocols using the diamond NV center rely both on lattice expansion and electron-phonon interactions [36], the measured CTE value of these nanoparticles can also contribute to a more complete understanding of quantum nanoscale temperature sensing in SiC. In this context, direct measurement of lattice parameters of nanoscale particles that come from BCDI measurements can be used in conjunction with the local strain map and with theory to better understand the process of thermometry, especially when the approach is applied to other promising polymorphs of SiC [37].

VI. SUMMARY

We show that the internal strain fields present in low-cost commercially available 3C-SiC nanoparticles can be significantly homogenized by high temperature annealing such that the nanoparticles become more suitable hosts as potential

quantum sensors. The improved strain, measured with *in situ* synchrotron-based Bragg coherent diffraction imaging of the particles, was found to persist to room temperature for all particles annealed to temperatures greater than 600 °C. This temperature range corresponds to temperatures where point defects have been found to anneal in bulk 3C-SiC and other polytypes, and thus we attribute the observed strain healing to the annihilation of mobile point defects. We support this hypothesis with an analysis of the strain distribution of the outer 100-nm-deep particle surface layer as compared to the inner volume and with Raman spectroscopy that together indicate that surface-mediated processes do not play a role in the observed strain annealing. Finally, we derive values of the average room temperature lattice parameter and the coefficient of thermal expansion from the Bragg peak positions of the particles, relevant to thermometry via quantum sensing.

Importantly, this work also establishes the feasibility of performing BCDI at high temperatures (up to 900 °C) to map structural hystereses relevant to the processing of quantum nanomaterials. Further, it points the way towards more comprehensive BCDI experiments that reveal the mechanisms of strain annealing in more detail, for example, by imaging the full strain 3D strain tensor enabled by improvements in BCDI-compatible *in situ* hardware.

Our results provide insight into effective annealing protocols and possible strain relaxation mechanisms of 3C SiC nanoparticles. These nanoparticle imaging techniques could also benefit applications where the understanding of particle morphology becomes important, such as in biosensing and nanoabrasives. The improvements in strain homogeneity as a function of temperature can also shed light as to processing strategies of bulk and nanofabricated devices of this and other SiC polymorphs, and impact specific areas such as improving quantum efficiency and reducing local strain inhomogeneities for broader quantum technologies.

ACKNOWLEDGMENTS

Experimental design, *in situ* BCDI measurements of SiC nanoparticles, image phase retrieval, data reduction, analysis, and interpretation was supported by the US Department of Energy, Office of Science, Basic Energy Sciences, Materials Sciences and Engineering Division. Use of the Advanced Photon Source was supported by the US Department of Energy, Office of Science, Office of Basic Energy Sciences, under Contract No. DE-AC02-06CH11357. Sample preparation and SEM characterization was supported by ARO Grant No. W911NF-15-2-0058 and made use of the Pritzker Nanofabrication Facility of the Institute for Molecular Engineering at the University of Chicago, which receives support from Soft and Hybrid Nanotechnology Experimental (SHyNE) Resource (NSF ECCS-1542205), a node of the National Science Foundation's National Nanotechnology Coordinated Infrastructure. We made use of shared Raman spectroscopy facilities supported by the NSF MRSEC Program under DMR0820054. C.P.A. was supported by the Department of Defense (DoD) through the National Defense Science & Engineering Graduate Fellowship (NDSEG) Program.

APPENDIX

Here, we present additional information including BCDI images before and after annealing (Fig. 7), the complete hysteresis plots for all particles (Figs. 8 and 9), and scanning electron microscopy images of before and after annealing (Fig. 10). Also included are the results from the Raman measurements referenced in the main text (Fig. 11).

Figure 7 shows the final and initial 3D morphology of particles 1 to 5 (gray isosurfaces), as well as a cut through the centers of each particle that show a two-dimensional (2D) cut of the spatial distribution of strain at room temperature and at the maximum annealing temperature for each particle. We note that in particles annealed to temperatures above 500 °C, the morphology of the final state is smoother than that of the initial state. This smoothing was also observed by comparing pre and postannealed SiC BCDI samples with scanning electron microscopy (SEM), shown in Fig. 10.

A plot of all the strain hysteresis curves is shown in Fig. 8. This same strain data are also plotted as a function of time in Fig. 9 where the coloration of the data points correspond to the measurement temperature.

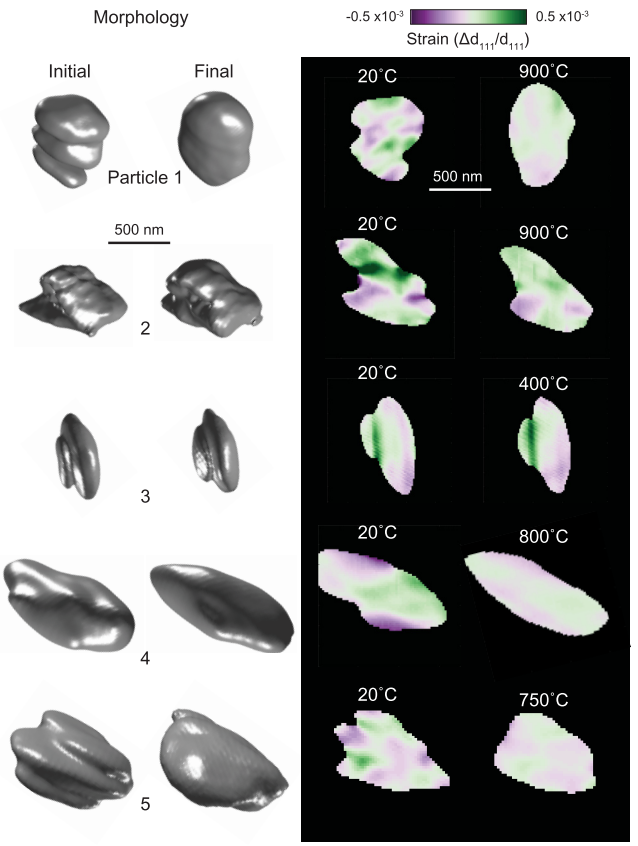

FIG. 7. The 3D morphology of all particles in their initial and final states (left columns), and cuts through the interior strain fields (right columns) at room temperature and at the maximum annealing temperature.

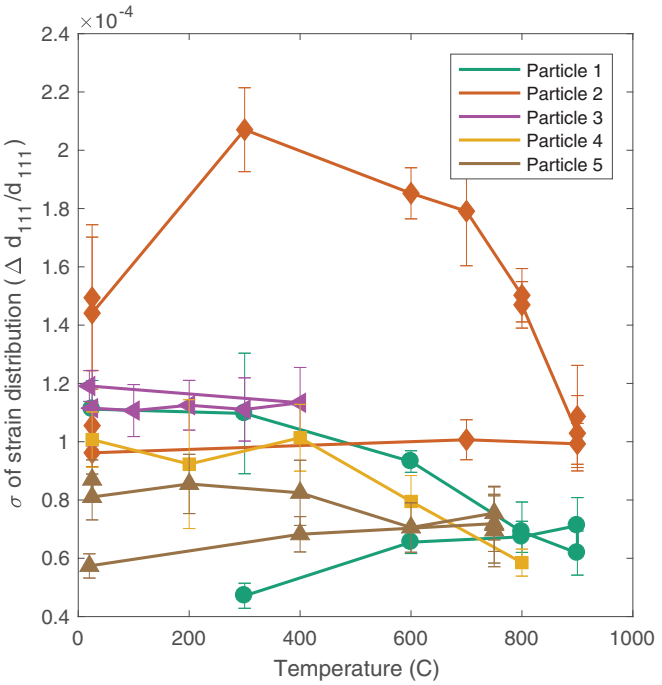

FIG. 8. Temperature/strain hysteresis is shown for all particles in this study. The hysteresis loops of Particles 1 and 5 are shown individually in Fig. 3.

Here, we point out that an increase in strain was seen in Particle 2 between room temperature and 300 °C. This strain behavior was not observed in any other particle, and may be connected to surface effects on this particular sample.

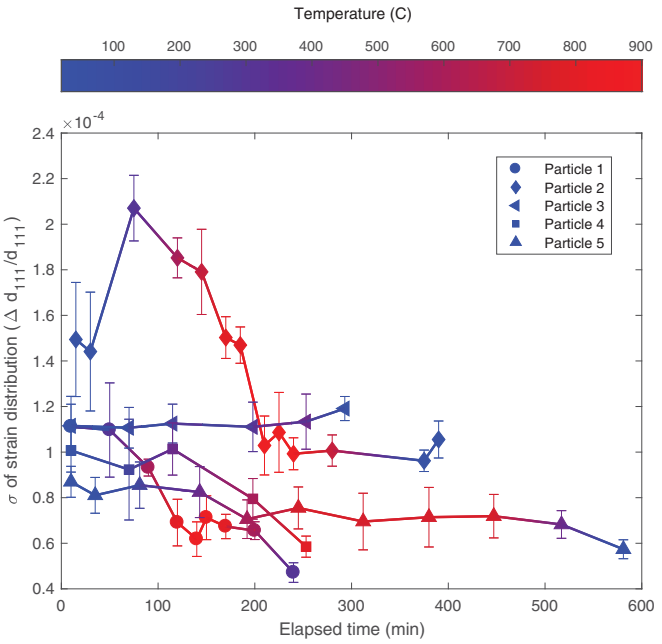

FIG. 9. The annealing behavior of all five particles in this study, showing the strain homogeneity as a function of time (x axis) and temperature (color). All particles show a decrease in overall strain above 500 °C, with particle 3 showing no change in strain going only up to 400 °C.

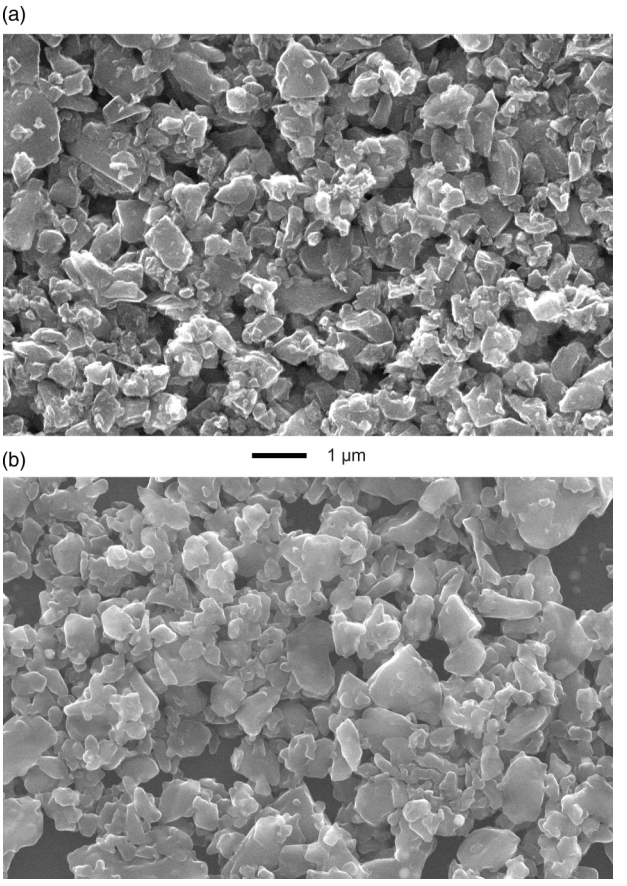

FIG. 10. (a) An SEM image of an as-prepared Si substrate coated with SiC nanoparticles for BCDI study. (b) An SEM image of another such sample after annealing to 800 °C. Particle 4 in this study was measured from this substrate.

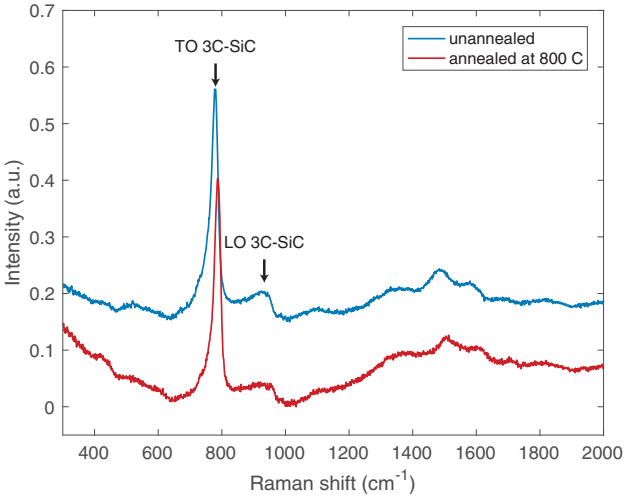

FIG. 11. Ensemble Raman measurements were done of pre-annealed and post-annealed SiC samples for BCDI measurements (offset for clarity) with transverse (TO) and longitudinal (LO) optical phonons at ∼780 cm^{-1} and ∼930 cm^{-1} respectively. There does not appear to be an appreciable difference in the two spectra, and, notably, no signature of carbonization is present in either case, indicating that this process did not play a role in the strain annealing behavior observed with BCDI.

[1] C. E. Weitzel, J. W. Palmour, C. H. Carter, K. Moore, K. J. Nordquist, S. Alien, C. Thero, and M. Bhatnagar, Silicon carbide high-power devices, IEEE Trans. Electron Devices **43**, 1732 (1996).

[2] X. She, A. Q. Huang, O. Lucia, and B. Ozpineci, Review of silicon carbide power devices and their applications, IEEE Trans. Ind. Electron. **64**, 8193 (2017).

[3] M. Mehregany, C. A. Zorman, N. Rajan, and Chien Hung Wu, Silicon carbide MEMS for harsh environments, Proc. IEEE **86**, 1594 (1998).

[4] T. Kimoto and J. A. Copper, *Fundamentals of Silicon Carbide Technology Growth, Characterization, Devices, and Applications* (Wiley, New York, 2014).

[5] S. Castelletto, B. C. Johnson, C. Zachreson, D. Beke, I. Balogh, T. Ohshima, I. Aharonovich, and A. Gali, Room temperature quantum emission from cubic silicon carbide nanoparticles, ACS Nano **8**, 7938 (2014).

[6] E. Janzén, A. Gali, P. Carlsson, A. Gällström, B. Magnusson, and N. T. Son, The silicon vacancy in SiC, Physica B: Condensed Matter **404**, 4354 (2009).

[7] W. F. Koehl, B. B. Buckley, F. J. Heremans, G. Calusine, and D. D. Awschalom, Room temperature coherent control of defect spin qubits in silicon carbide, Nature **479**, 84 (2011).

[8] F. J. Heremans, C. G. Yale, and D. D. Awschalom, Control of spin defects in wide-bandgap semiconductors for quantum technologies, Proc. IEEE **104**, 2009 (2016).

[9] R. Schirhagl, K. Chang, M. Loretz, and C. L. Degen, Nitrogen-vacancy centers in diamond: Nanoscale sensors for physics and biology, Annu. Rev. Phys. Chem. **65**, 83 (2014).

[10] C. L. Degen, F. Reinhard, and P. Cappellaro, Quantum sensing, Rev. Mod. Phys. **89**, 035002 (2017).

[11] L. S. Ramsdell, Studies on silicon carbide, Am. Mineral. **32**, 64 (1947).

[12] O. Madelung, *Semiconductors - Basic Data* (Springer, New York, 1996).

[13] G. L. Harris, *Properties of Silicon Carbide*, INSPEC (Plenum, New York, 1995).

[14] A. L. Falk, B. B. Buckley, G. Calusine, W. F. Koehl, V. V. Dobrovitski, A. Politi, C. A. Zorman, P. X.-L. Feng, and D. D. Awschalom, Polytype control of spin qubits in silicon carbide, Nat. Commun. **4**, 1819 (2013).

[15] M. W. Doherty, N. B. Manson, P. Delaney, F. Jelezko, J. Wrachtrup, and L. C. L. Hollenberg, The nitrogen-vacancy color center in diamond, Phys. Rep. **528**, 1 (2013).

[16] E. Bernardi, R. Nelz, S. Sonusen, and E. Neu, Nanoscale sensing using point defects in single-crystal diamond: Recent progress on nitrogen vacancy center-based sensors, Crystals **7**, 124 (2017).

[17] D. J. Christle, P. V. Klimov, C. F. de las Casas, K. Szász, V. Ivády, V. Jokubavicius, J. Ul Hassan, M. Syvajarvi, W. F. Koehl, T. Ohshima, N. T. Son, E. Janzén, A. Gali, and D. D. Awschalom, Isolated Spin Qubits in SiC with a High-Fidelity Infrared Spin-to-Photon Interface, Phys. Rev. X **7**, 021046 (2017).

[18] C. F. de las Casas, D. J. Christle, J. U. Hassan, T. Ohshima, N. T. Son, and D. D. Awschalom, Stark tuning and electrical charge state control of single divacancies in silicon carbide, Appl. Phys. Lett. **111**, 262403 (2017).

[19] J. Choi and N. S. Wang, Nanoparticles in biomedical applications and their safety concerns, in *Biomedical Engineering - From Theory to Applications*, edited by R. Fazel-Rezai (InTech, Rijeka, 2011), Chap. 13, pp. 299–314.

[20] S. O. Hruszkewycz, W. Cha, P. Andrich, C. P. Anderson, A. Ulvestad, R. Harder, P. H. Fuoss, D. D. Awschalom, and F. J. Heremans, *In situ* study of annealing-induced strain relaxation in diamond nanoparticles using Bragg coherent diffraction imaging, APL Mater. **5**, 026105 (2017).

[21] I. Robinson and R. Harder, Coherent X-ray diffraction imaging of strain at the nanoscale, Nat. Mater. **8**, 291 (2009).

[22] A. Ulvestad, M. J. Welland, S. S. E. Collins, R. Harder, E. Maxey, J. Wingert, A. Singer, S. Hy, P. Mulvaney, P. Zapol, and O. G. Shpyrko, Avalanching strain dynamics during the hydriding phase transformation in individual palladium nanoparticles, Nat. Commun. **6**, 10092 (2015).

[23] H. Itoh, A. Kawasuso, T. Ohshima, M. Yoshikawa, I. Nashiyama, S. Tanigawa, S. Misawa, H. Okumura, and S. Yoshida, Intrinsic defects in cubic silicon carbide, Phys. Status Solidi A **162**, 173, (1997).

[24] N. T. Son, P. N. Hai, and E. Janzén, Carbon vacancy-related defect in 4 *H* and 6 *H* SiC, Phys. Rev. B **63**, 201201 (2001).

[25] M. Bockstedte, A. Mattausch, and O. Pankratov, *Ab initio* study of the migration of intrinsic defects in 3*C*−SiC, Phys. Rev. B **68**, 205201 (2003).

[26] A. Uedono, H. Itoh, T. Ohshima, R. Suzuki, T. Ohdaira, S. Tanigawa, Y. Aoki, M. Yoshikawa, I. Nashiyama, T. Mikado, H. Okumura, and S. Yoshida, Annealing properties of defects in ion-implanted 3C-SiC studied using monoenergetic positron beams, Jpn. J. Appl. Phys. **36**, 6650 (1997).

[27] C. S. Roper, V. Radmilovic, R. T. Howe, and R. Maboudian, Effects of annealing on residual stress and strain gradient of doped polycrystalline SiC thin films, Electrochem. Solid State Lett. **11**, D35, (2008).

[28] T. Lingner, S. Greulich-Weber, J.-M. Spaeth, U. Gerstmann, E. Rauls, Z. Hajnal, T. Frauenheim, and H. Overhof, Structure of the silicon vacancy in 6*H*−SiC after annealing identified as the carbon vacancy–carbon antisite pair, Phys. Rev. B **64**, 245212 (2001).

[29] A. Ulvestad, A. Singer, J. N. Clark, H. M. Cho, J. W. Kim, R. Harder, J. Maser, Y. S. Meng, and O. G. Shpyrko, Topological defect dynamics in operando battery nanoparticles, Science **348**, 1344 (2015).

[30] A. Ulvestad, J. N. Clark, R. Harder, I. K. Robinson, and O. G. Shpyrko, 3D imaging of twin domain defects in gold nanoparticles, Nano Lett. **15**, 4066 (2015).

[31] F. Hofmann, D. Nguyen-Manh, M. R. Gilbert, C. E. Beck, J. K. Eliason, A. A. Maznev, W. Liu, D. E. J. Armstrong, K. A. Nelson, and S. L. Dudarev, Lattice swelling and modulus change in a helium-implanted tungsten alloy: X-ray micro-diffraction, surface acoustic wave measurements, and multiscale modelling, Acta Mater. **89**, 352 (2015).

[32] F. Hofmann, E. Tarleton, R. J. Harder, N. W. Phillips, P.-W. Ma, J. N. Clark, I. K. Robinson, B. Abbey, W. Liu, and C. E. Beck, 3D lattice distortions and defect structures in ion-implanted nano-crystals, Sci. Rep. **7**, 45993 (2017).

[33] T. Liao, G. Roma, and J. Wang, First-principles study of neutral silicon interstitials in 3C- and 4H-SiC, Philos. Mag. **89**, 2271 (2009).

[34] J. Ruska, L. J. Gauckler, J. Lorenz, and H. U. Rexer, The quantitative calculation of SiC polytypes from measurements

of X-ray diffraction peak intensities, J. Mater. Sci. **14**, 2013 (1979).

[35] D. N. Talwar and J. C. Sherbondy, Thermal expansion coefficient of 3C–SiC, Appl. Phys. Lett. **67**, 3301 (1995).

[36] M. W. Doherty, V. M. Acosta, A. Jarmola, M. S. J. Barson, N. B. Manson, D. Budker, and L. C. L. Hollenberg, Temperature shifts of the resonances of the NV^- center in diamond, Phys. Rev. B **90**, 041201(R) (2014).

[37] H. Kraus, V. A. Soltamov, F. Fuchs, D. Simin, A. Sperlich, P. G. Baranov, G. V. Astakhov, and V. Dyakonov, Magnetic field and temperature sensing with atomic-scale spin defects in silicon carbide, Sci. Rep. **4**, 5303 (2014).